

SOFTENING AND SNAP-BACK INSTABILITY IN COHESIVE SOLIDS

ALBERTO CARPINTERI

Department of Structural Engineering, Politecnico di Torino, 10129 Torino, Italy

SUMMARY

The nature of the crack and the structure behaviour can range from ductile to brittle, depending on material properties, structure geometry, loading condition and external constraints. The influence of variation in fracture toughness, tensile strength and geometrical size scale is investigated on the basis of the π -theorem of dimensional analysis. Strength and toughness present in fact different physical dimensions and any consistent fracture criterion must describe energy dissipation per unit of volume and per unit of crack area respectively. A cohesive crack model is proposed aiming at describing the size effects of fracture mechanics, i.e. the transition from ductile to brittle structure behaviour by increasing the size scale and keeping the geometrical shape unchanged.

For extremely brittle cases (e.g. initially uncracked specimens, large and/or slender structures, low fracture toughness, high tensile strength, etc.) a snap-back instability in the equilibrium path occurs and the load–deflection softening branch assumes a positive slope. Both load and deflection must decrease to obtain a slow and controlled crack propagation (whereas in normal softening only the load must decrease). If the loading process is deflection-controlled, the loading capacity presents a discontinuity with a negative jump. It is proved that such a catastrophic event tends to reproduce the classical LEFM-instability ($K_I = K_{IC}$) for small fracture toughnesses and/or for large structure sizes. In these cases, neither the plastic zone develops nor slow crack growth occurs before unstable crack propagation.

INTRODUCTION

Crack growth in real structures is often stable and develops slowly with initially partial and then total stress-relaxation at the crack tip. Only in some particular cases, do crack formation and/or propagation occur suddenly with a catastrophic drop in the load carrying capacity. The nature of the crack and structure behaviour can range from ductile to brittle, depending on material properties, structure geometry, loading condition and external constraints. The influence of variation in fracture toughness, tensile strength and geometrical size scale may be investigated on the basis of the π -theorem of dimensional analysis.^{1–3} Strength and toughness parameters present in fact different physical dimensions and any consistent fracture criterion and numerical model must describe energy dissipation per unit of volume and per unit of crack area respectively.⁴

When the fracture phenomenon is extremely brittle and only energy dissipation on the crack surfaces occurs, LEFM may be properly applied to describe the catastrophic structure behaviour. On the other hand, when the fracture process is extremely ductile and only energy dissipation in the ligament volume develops, perfectly plastic limit analysis may be conveniently used. The problem arises for the intermediate cases, when the fracture process is initially ductile and then brittle and the crack propagation is initially slow and then fast and uncontrollable. In those cases, a suitable fracture model must be adopted. In the present paper a *cohesive crack model* is

proposed with the aim of describing the size effects of fracture mechanics, i.e. the transition from ductile to brittle structure behaviour only by increasing the size scale and keeping the geometrical shape unchanged.

For extremely brittle cases (e.g. initially uncracked specimens, large and/or slender structures, low fracture toughness, high tensile strength, etc.) a snap-back instability in the equilibrium path occurs and the load P -deflection δ softening branch assumes a positive slope ($dP/d\delta > 0$). This means that both load and deflection must decrease to obtain slow and controlled crack propagation, whereas in normal softening ($dP/d\delta < 0$) only the load must decrease. If, in the former situation, the loading process is deflection-controlled, the P - δ curve presents a discontinuity and the representative point drops on the lower branch with negative slope.

Snap-back instability has been studied by several authors: Maier,⁵ Bažant,⁶ Carpinteri,⁷ Crisfield,⁸ Schreyer and Chen,⁹ Rots *et al.*,¹⁰ among others. On the other hand, the object of the present paper is to put it in the content of the LEFM-instability. From an experimental point of view, snap-back instability was originally detected by Fairhurst *et al.*¹¹ in the compressive behaviour of rocks and more recently by Rokugo *et al.*¹² and Biolzi *et al.*¹³ in the bending behaviour of concrete.

The accuracy of the numerical description of cohesive crack propagation is also investigated. It is shown that, when the finite element mesh is too coarse, i.e. when the cohesive forces are too far from each other, the cohesive model is unable to describe the fracture process. In other words, when the structure is very large or the fracture toughness very small, the plastic or cohesive zone at the crack tip becomes relatively small and the finite element mesh must be refined, so that such a zone and the LEFM-stress-singularity can be reproduced and the equilibrium branching described.

For each critical value of strain energy release rate \mathcal{G}_{IC} , an upper bound to the finite element size does exist, beyond which the numerical response is unstable. Conversely, for each finite element size a lower bound to \mathcal{G}_{IC} does exist, below which the P - δ curve is not reproducible. Such considerations are extended to the non-dimensional field and it is shown that, for low fracture toughness and/or large structure sizes, the loading capacity can be provided by the well-known condition $K_I = K_{IC}$. In these cases it is not convenient to use a cohesive crack model with a large number of finite elements. It is much more economical to apply a LEFM code with the stress-singularity embedded at the crack tip.

COHESIVE CRACK MODEL

The cohesive crack model is a representative model when the plastic zone is confined to a very narrow band. The plastic stress field is represented by restraining forces which close the crack tip faces. These forces are non-increasing functions of the distance between the crack surfaces.

Such a model was originally proposed by Barenblatt,¹⁴ who considered the cohesive forces confined to an interaction zone of constant size, with the shape of the terminal crack region being fixed, even if translation was occurring. On the other hand, Dugdale¹⁵ considered a similar model with vanishing singularity at the crack tip and an interaction zone of variable size, spreading into the entire ligament at the condition of general yielding.

In the following years cohesive crack models were reconsidered, with some modifications, by several authors: Bilby *et al.*,¹⁶ Rice,¹⁷ Wnuk,¹⁸ Hillerborg *et al.*,¹⁹ Ingraffea,²⁰ among others.

The present cohesive crack model is based on the following assumptions.^{7, 19, 21-23}

1. The cohesive fracture zone (plastic or process zone) begins to develop when the maximum principal stress achieves the ultimate tensile strength σ_u (Figure 1(a)).

2. The material in the process zone is partially damaged but still able to transfer stress. Such a stress is dependent on the crack opening displacement w (Figure 1(b)).

The *real crack tip* is defined as the point where the distance between the crack surfaces is equal to the critical value of crack opening displacement w_c and the normal stress vanishes (Figure 2(a)). On the other hand, the *fictitious crack tip* is defined as the point where the normal stress attains the maximum value σ_u and the crack opening vanishes (Figure 2(a)).

The closing stresses acting on the crack surfaces (Figure 2(a)) can be replaced by nodal forces (Figure 2(b)). The intensity of these forces depends on the opening of the fictitious crack, w , according to the σ - w constitutive law of the material (Figure 1(b)). When the tensile strength σ_u is achieved at the fictitious crack tip (Figure 2(b)), the top node is opened and a cohesive force starts acting across the crack, while the fictitious crack tip moves to the next node.

With reference to the single edge notched beam (SENB) geometry in Figure 3, the nodes are distributed along the potential fracture line. It is impossible to extend the fracture nodes to the whole cross-section depth, as would be required to follow the fracture process up to the complete load relaxation, since a sufficiently large ligament is needed to guarantee a correct structural analysis. A ligament equal to one tenth of the depth ($b/10$) is assumed.

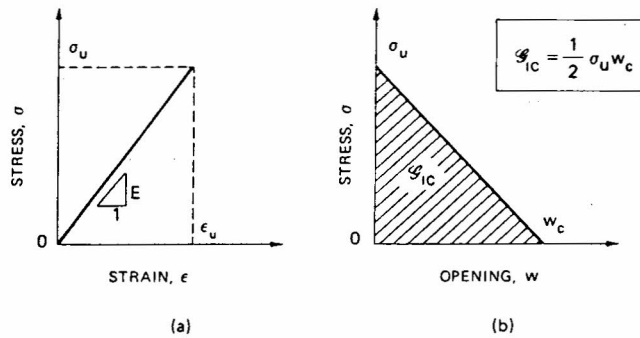


Figure 1. Stress-strain (a) and stress-crack opening displacement (b) constitutive laws

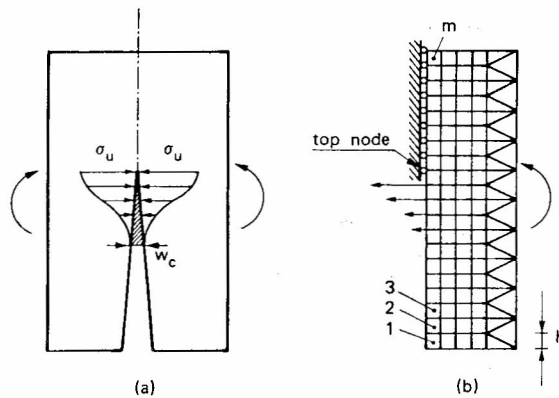


Figure 2. Stress distribution across the cohesive zone (a) and equivalent nodal forces in the finite element mesh (b)

The coefficients of influence in terms of node openings and deflection are computed by a finite element analysis (quadrilateral isoparametric elements with linear shape functions) where the fictitious structure in Figure 3 is subjected to $(n + 1)$ different loading conditions. Consider the SENB in Figure 4(a) with the initial crack tip in the node k . The crack opening displacements at the n fracture nodes may be expressed as follows:

$$\mathbf{w} = \mathbf{K}\mathbf{F} + \mathbf{C}\mathbf{P} + \mathbf{\Gamma} \quad (1)$$

where

\mathbf{w} = vector of the crack opening displacements,

\mathbf{K} = matrix of the coefficients of influence (nodal forces),

\mathbf{F} = vector of the nodal forces,

\mathbf{C} = vector of the coefficients of influence (external load),

\mathbf{P} = external load,

$\mathbf{\Gamma}$ = vector of the crack opening displacements due to the specimen weight.

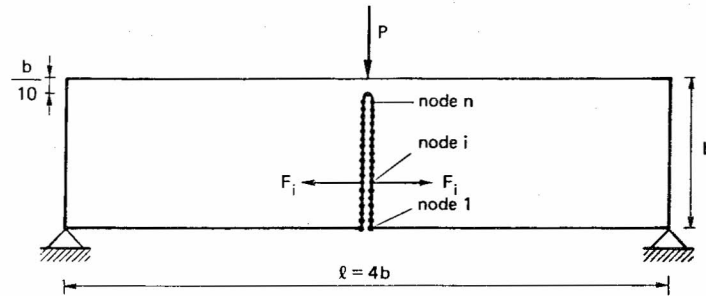


Figure 3. Finite element nodes along the potential fracture line

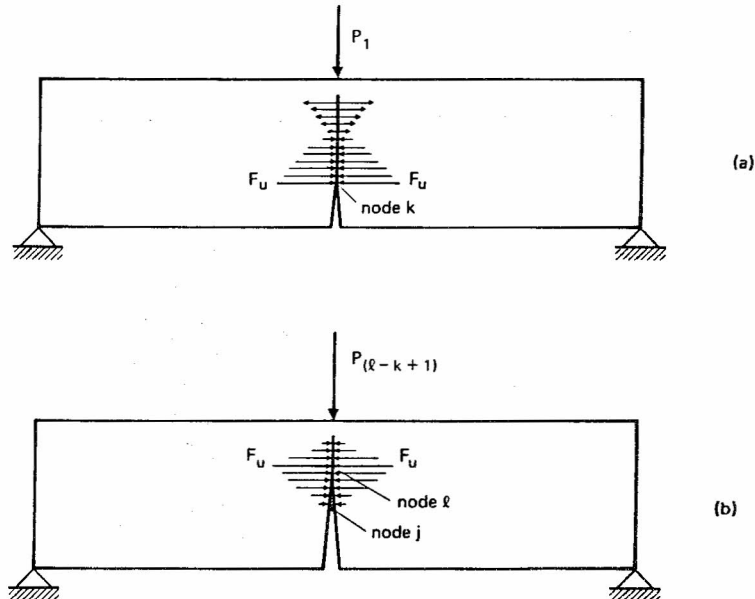


Figure 4. Cohesive crack configurations at the first (a) and $(l - k + 1)$ th (b) crack growth increment

On the other hand, the initial crack is stress-free and therefore

$$F_i = 0, \quad \text{for } i = 1, 2, \dots, (k-1) \quad (2a)$$

while at the ligament there is no displacement discontinuity:

$$w_i = 0, \quad \text{for } i = k, (k+1), \dots, n \quad (2b)$$

Equations (1) and (2) constitute a linear algebraical system of $2n$ equations and $2n$ unknowns, i.e. the elements of vectors \mathbf{w} and \mathbf{F} . If load P and vector \mathbf{F} are known, it is possible to compute the beam deflection, δ :

$$\delta = \mathbf{C}^T \mathbf{F} + D_P P + D_\gamma \quad (3)$$

where D_P is the deflection for $P = 1$ and D_γ is the deflection due to the specimen weight.

After the first step, a cohesive zone forms in front of the real crack tip (Figure 4(b)), say between nodes j and l . Then equations (2) are replaced by

$$F_i = 0, \quad \text{for } i = 1, 2, \dots, (j-1) \quad (4a)$$

$$F_i = F_u \left(1 - \frac{w_i}{w_c} \right), \quad \text{for } i = j, (j+1), \dots, l \quad (4b)$$

$$w_i = 0, \quad \text{for } i = l, (l+1), \dots, n \quad (4c)$$

where F_u is the ultimate strength nodal force:

$$F_u = 0.9b\sigma_u/n \quad (5)$$

Equations (1) and (4) constitute a linear algebraical system of $(2n+1)$ equations and $(2n+1)$ unknowns, i.e. the elements of vectors \mathbf{w} and \mathbf{F} and the external load P .

At the first step, the cohesive zone is missing ($l = j = k$) and the load P_1 producing the ultimate strength nodal force F_u at the initial crack tip (node k) is computed. Such a value P_1 , together with the related deflection δ_1 computed through equation (3), gives the first point of the P - δ curve. At the second step, the cohesive zone is between the nodes k and $(k+1)$, and the load P_2 producing the force F_u at the second fictitious crack tip (node $k+1$) is computed. Equation (3) then provides the deflection δ_2 . At the third step, the fictitious crack tip is in the node $(k+2)$, and so on. *The present numerical program simulates a loading process where the controlling parameter is the fictitious crack depth.* On the other hand, real (or stress-free) crack depth, external load and deflection are obtained at each step after an iterative procedure.

The program stops with the untying of the node n and, consequently, with the determination of the last couple of values F_n and δ_n . In this way, the complete load-deflection curve is automatically plotted by the computer.

NUMERICAL ACCURACY IN FINITE ELEMENT ANALYSIS

For any non-linear crack model it is possible to define a non-dimensional number able to measure the structural brittleness (or ductility). More generally, we can say that, once tensile strength and fracture toughness of the material are defined, it is possible to deduce a brittleness (or ductility) number, such material properties presenting different physical dimensions with respect to the length. The size scale, raised to some suitable power, is therefore included in this number. Such concepts based on dimensional analysis and physical similitude were exposed in

two early papers by the writer.^{1,2} On that occasion, the (stress) brittleness number was defined as follows:

$$s = \frac{K_{IC}}{\sigma_y b^{1/2}} \quad (6a)$$

for elastic–perfectly plastic materials, where σ_y = tensile yield strength, K_{IC} = critical stress-intensity factor, b = size scale, or

$$s = \frac{K_{IC}}{\sigma_u b^{1/2}} \quad (6b)$$

for elastic–perfectly brittle materials, where σ_u = tensile ultimate strength.

Some years later, the writer introduced the energy brittleness number concept⁷

$$s_E = \frac{\mathcal{G}_{IC}}{\sigma_u b} \quad (7)$$

where $\mathcal{G}_{IC} = \frac{1}{2} \sigma_u w_c$ is the area under the σ – w curve in Figure 1(b) and represents the energy necessary to create a unit crack surface. When the cohesive σ – w law is linear, the brittleness number s_E can be put also in the simpler form

$$s_E = \frac{w_c}{2b} \quad (8)$$

which is the ratio of the critical crack opening displacement w_c to the characteristic structure size $2b$.

Recalling the quadratic relationship between critical stress-intensity factor K_{IC} and fracture energy \mathcal{G}_{IC} :

$$\mathcal{G}_{IC} = \frac{K_{IC}^2}{E} \quad (\text{plane stress}) \quad (9)$$

we can correlate the two brittleness numbers s_E and s :

$$s_E = \varepsilon_u s^2 \quad (10)$$

where ε_u is the ultimate tensile dilatation and s^2 is interpretable also as the Hillerborg brittleness number, $s^2 = l_{CH}/b$, the characteristic length being defined as¹⁹

$$l_{CH} = \frac{\mathcal{G}_{IC} E}{\sigma_u^2} \quad (11)$$

On the basis of a rigorous dimensional analysis of the problem, we expect the same dimensionless load–deflection curve, $P/\sigma_u b^2$ versus δ/b , only if two of the numbers s_E , s , ε_u in equation (10) are the same.

It is of interest to mention that, subsequently, other brittleness numbers were defined in the framework of the strain energy density theory of Sih (Carpinteri and Sih⁴) and, very recently, of the crack band model of Bažant (Bažant and Pfeiffer²⁴). All these numbers are substantially equivalent in the description of size effects and the associated transition from ductile behaviour to brittle LFM behaviour.

The three point bending beam in Figure 3 is considered herein, with constant geometrical proportions: span = $l = 4b$, thickness = $t = b$. The scale factor is therefore represented by the beam depth b .

As is shown in Figure 2(b), m finite elements are adjacent to the central line, whereas only $n = 0.9m$ nodes can be untied during the crack growth (Figure 3). The finite element size h (Figure 2(b)) is then connected with the beam depth b through the simple relation $b = mh$.

The three different finite element meshes in Figure 5 are considered. Mesh (a) presents 20 elements and 18 fracture nodes, mesh (b) 40 elements and 36 fracture nodes, mesh (c) 80 elements and 72 fracture nodes.

The load–deflection response of the three point bending beam in Figure 3 is represented in Figures 6(a), (b) and (c), for $m = 20, 40$ and 80 respectively. The initial crack depth is assumed to be $a_0/b = 0.3$, while the ultimate tensile strain $\epsilon_u = \sigma_u/E$ is 8.7×10^{-5} and Poisson's ratio $\nu = 0.1$. The diagrams are plotted in non-dimensional form by varying the brittleness number s_E . The simple variation in this dimensionless number reproduces all the cases related to the independent variations in \mathcal{G}_{IC} , b and σ_u . Not the single values of \mathcal{G}_{IC} , b and σ_u , but their function s_E —see equation (7)—is responsible for the structural behaviour, which can range from ductile to brittle. Specimens with high fracture toughness are then ductile, as well as small specimens and/or specimens with low tensile strength. Conversely, brittle behaviours are predicted for low fracture toughness, large specimens and/or high tensile strengths.

The influence of the variation in the number s_E is investigated over four orders of magnitude in Figures 6, from 2×10^{-2} to 2×10^{-5} . The results reported in Figures 6(a), (b) and (c) appear very

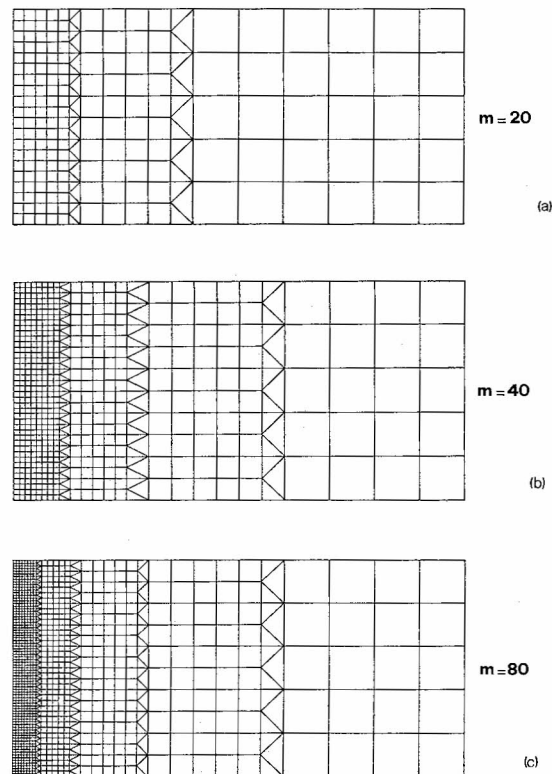


Figure 5. Refinement of the finite element mesh

similar. Of course, the diagrams for $m = 20$ (Figure 6(a)) are slightly less regular than those for $m = 80$ (Figure 6(c)), and present some weak cuspidal points, especially for low s_E numbers.

When ulteriorly lower s_E numbers are contemplated, the P - δ diagrams lose their regularity, from a mathematical point of view, and their resolution, from a graphical point of view. The

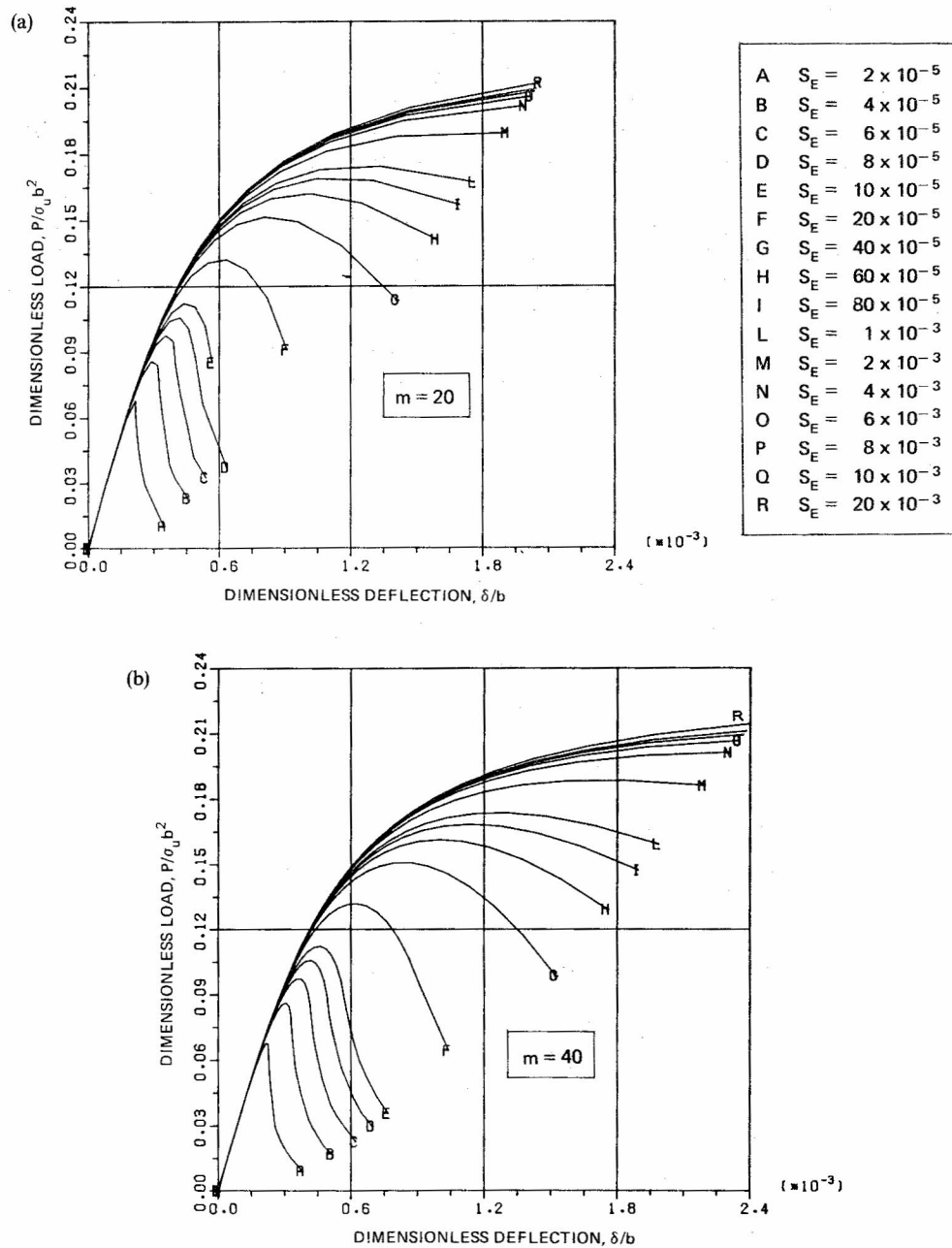


Figure 6(a) and (b) (Contd.)

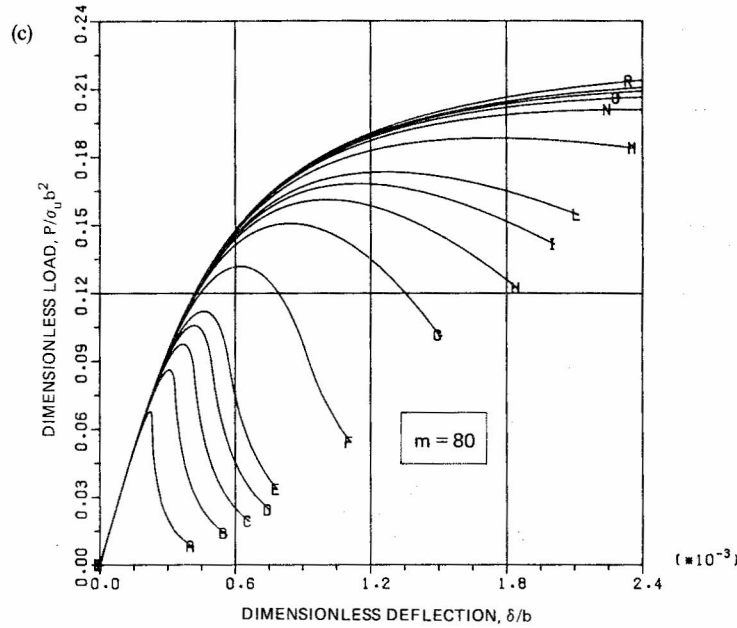


Figure 6. Dimensionless load-deflection plots by varying the brittleness number, $s_E = \mathcal{G}_{IC}/\sigma_u b = w_c/2b$, between 2×10^{-5} and 2×10^{-2} ; (a) $m = 20$; (b) $m = 40$; (c) $m = 80$

influence of the variation in the s_E number is further analysed over one order of magnitude in Figure 7, from 2×10^{-5} to 2×10^{-6} . The results reported in Figures 7(a), (b) and (c) appear much less uniform than those in Figures 6(a), (b) and (c). The diagrams for $m = 20$ (Figure 7(a)) are

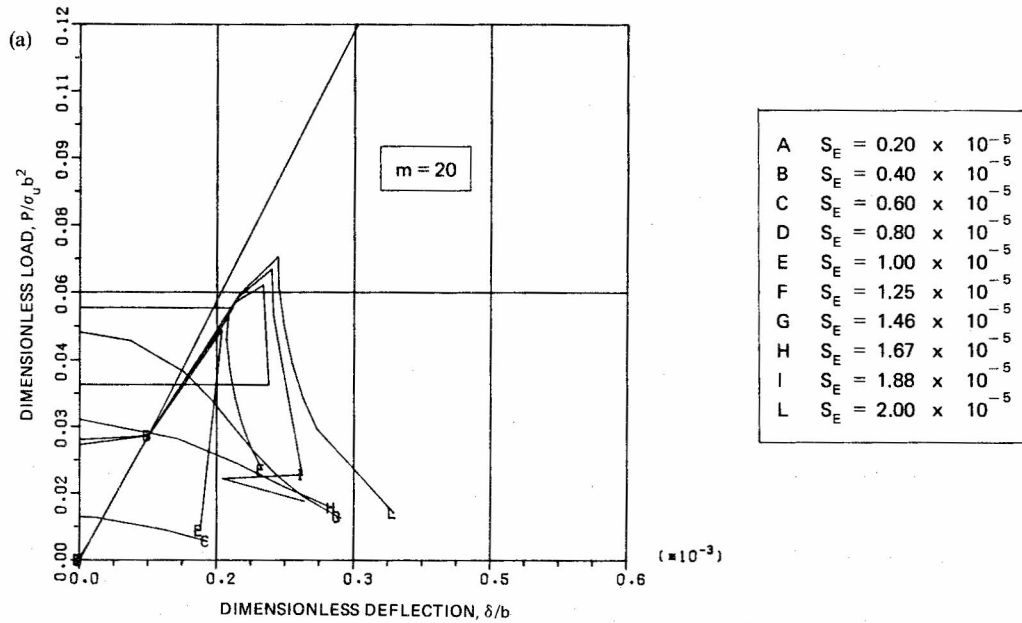


Figure 7(a) (Contd.)

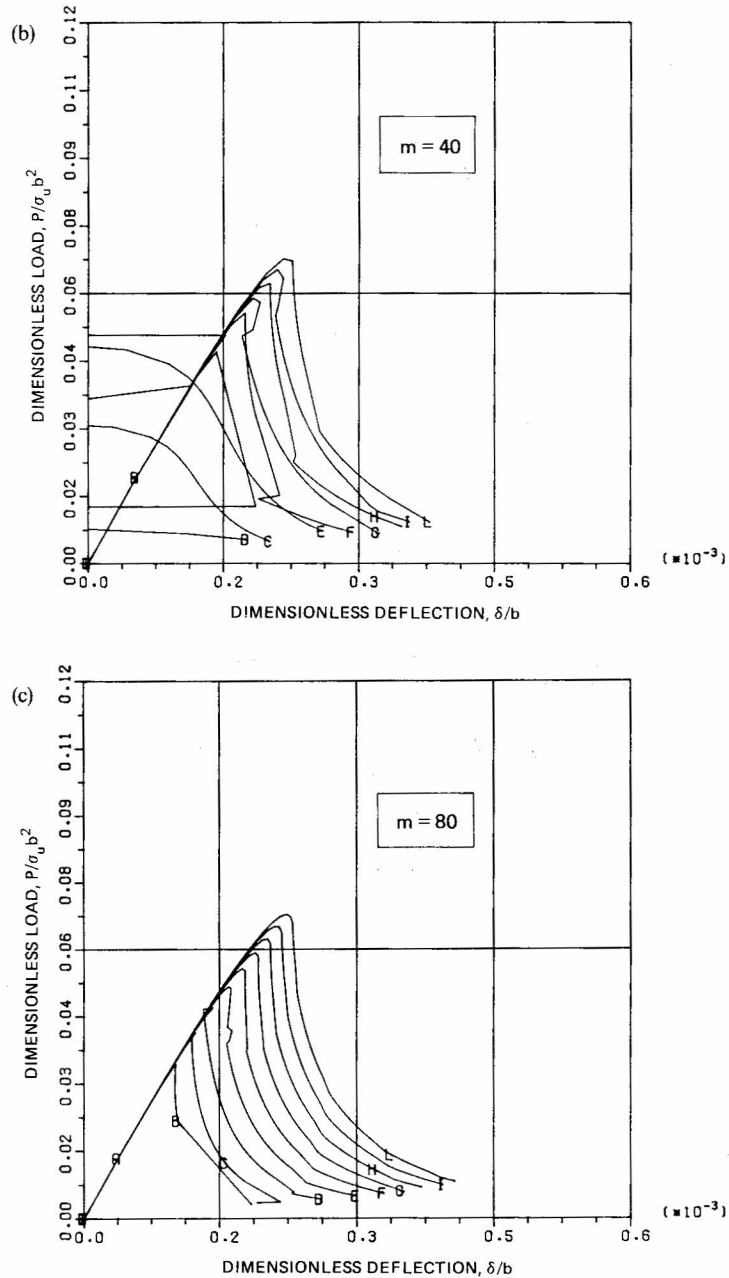


Figure 7. Dimensionless load-deflection plots by varying the brittleness number, $s_E = \mathcal{G}_{IC}/\sigma_u b = w_c/2b$, between 2×10^{-6} and 2×10^{-5} : (a) $m = 20$; (b) $m = 40$; (c) $m = 80$

lacking in mathematical regularity, graphical resolution and physical meaning. The diagrams present a slightly better regularity and resolution for $m = 40$ (Figure 7(b)), whereas, for $m = 80$ (Figure 7(c)), they appear sufficiently regular, especially for not too low brittleness numbers ($10^{-5} \lesssim s_E \lesssim 2 \times 10^{-5}$). If a better resolution is required for $2 \times 10^{-6} \lesssim s_E \lesssim 10^{-5}$, the mesh

must be refined, i.e. the number m increased. On the other hand, it is evident that the mesh must be refined, i.e. the cohesive forces must be closer, for relatively large structures and/or for relatively brittle materials, where the cohesive zone is confined to a small crack tip region.

From the cases shown in Figures 6 and 7, the s_E -threshold below which the results are unacceptable is approximately

$$s_E = \frac{w_c}{2mh} \approx \frac{80}{m} \times 10^{-5} \quad (12)$$

The lower bound to s_E can be regarded as an upper bound to the finite element size h :

$$h \lesssim 600w_c \quad (13)$$

For a normal concrete with maximum aggregate size of 2 cm, it is approximately $w_c \approx 0.1$ mm and then equation (13) gives $h \lesssim 6$ cm.

INFLUENCE OF THE INITIAL CRACK DEPTH

A three point bending test specimen of depth $b = 15$ cm, thickness $t = b = 15$ cm and span $l = 4b = 60$ cm is considered with an initial crack depth a_0/b . The finite element mesh in Figure 5(b) ($m = 40$) is utilized in the numerical simulation of a concrete-like material with the following mechanical properties: Young's modulus $E = 365,000$ kg/cm², tensile strength $\sigma_u = 31.90$ kg/cm², Poisson's ratio $\nu = 0.10$. For two different values of fracture toughness, $\mathcal{G}_{IC} = 0.05$ and 0.01 kg/cm respectively, the initial crack depth a_0/b is varied from 0.0 (initially uncracked specimen) to 0.5. For all the cases considered, the load-deflection (P - δ) and load-crack mouth opening displacement (P - w_1) curves are obtained.

The P - δ curves in Figure 8 are related to different initial crack depths. Obviously, stiffness and maximum loading capacity of the specimen decrease by increasing the initial crack depth a_0/b . On the other hand, even the slope of the softening branch decreases, so that the uncracked specimen reveals considerable instability and a nearly vertical drop in its loading capacity, whereas the cracked specimens appear much more ductile and controllable in the P - δ descending stage. The terminal softening branch appears to be totally independent of the initial crack depth. This is a direct consequence of the assumption of a damage zone collinear to the crack and concentrated on a line of zero thickness.

The P - δ curves in Figure 9 describe the specimen behaviour when $\mathcal{G}_{IC} = 0.01$ kg/cm. For $a_0/b \leq 0.25$ a snap-back behaviour occurs, that is, a softening branch with positive slope ($dP/d\delta > 0$) is revealed. If the loading process is controlled by the deflection, the loading capacity will show a discontinuity with a negative jump and the representative point will drop on the fourth branch of the P - δ curve (Figure 10). The part BD of the P - δ curve in Figure 10 appears as a virtual path, which can be revealed only by decreasing both load and deflection while the crack grows and opens. The four stages of the P - δ diagram in Figure 10 can be defined as follows:

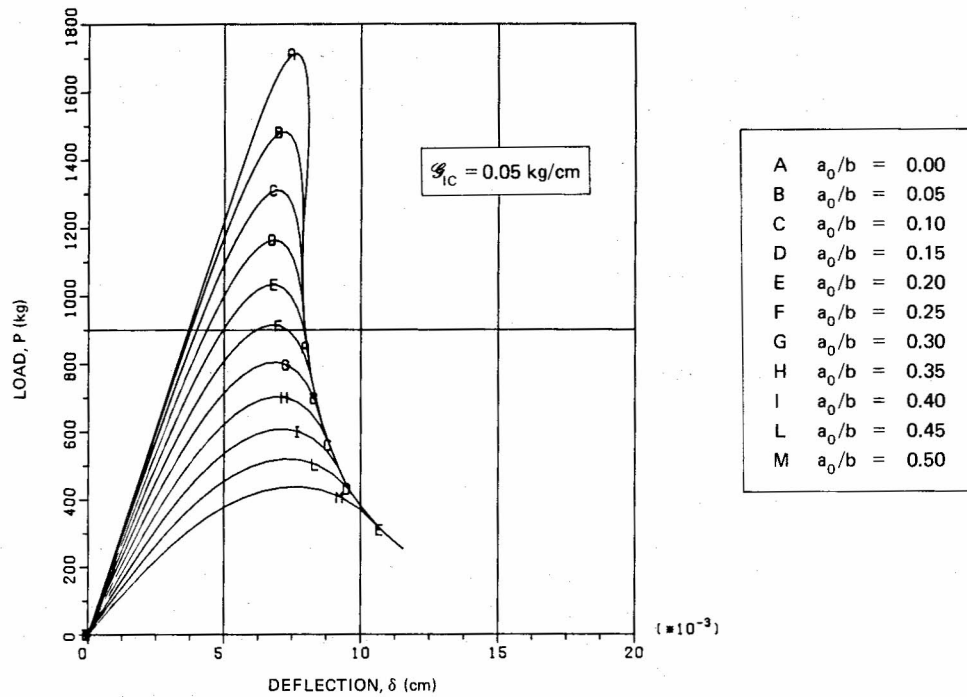
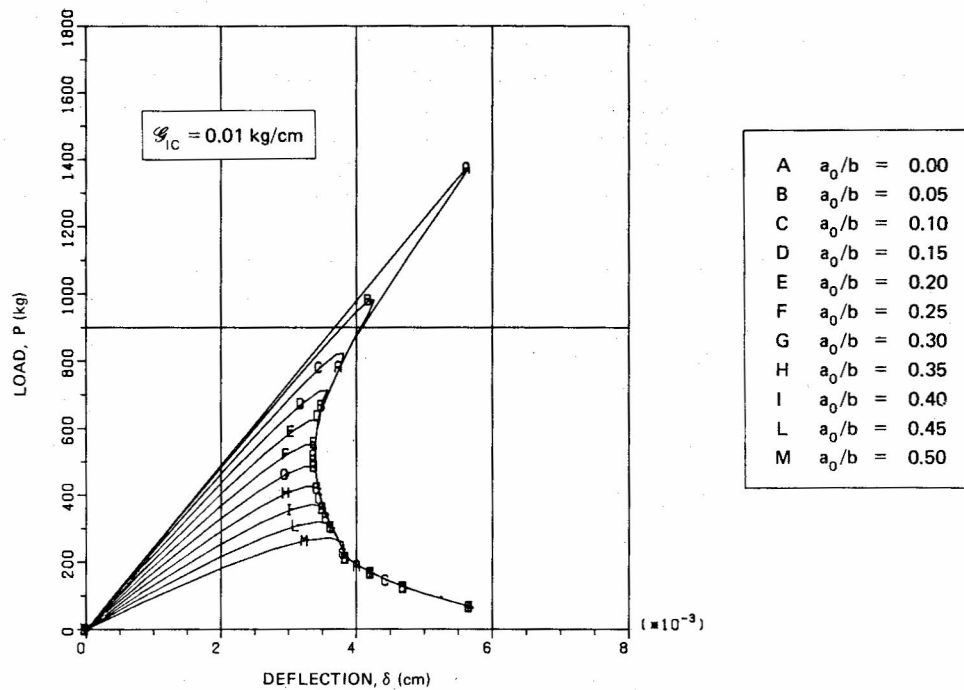
$$(OA) \quad \dot{P} > 0, \quad \dot{\delta} > 0, \quad \dot{a} \geq 0, \quad \dot{w}_1 \geq 0 \quad (14a)$$

$$(AB) \quad \dot{P} < 0, \quad \dot{\delta} > 0, \quad \dot{a} \geq 0, \quad \dot{w}_1 > 0 \quad (14b)$$

$$(BC) \quad \dot{P} < 0, \quad \dot{\delta} < 0, \quad \dot{a} > 0, \quad \dot{w}_1 > 0 \quad (14c)$$

$$(CD) \quad \dot{P} < 0, \quad \dot{\delta} > 0, \quad \dot{a} > 0, \quad \dot{w}_1 > 0 \quad (14d)$$

where the dot indicates derivative with respect to a quantity increasing monotonically with time (e.g. time itself or crack length). For the cases investigated numerically, points A and B tend to

Figure 8. Load-deflection plots by varying the initial crack depth a_0/b ($G_{IC} = 0.05 \text{ kg/cm}$)Figure 9. Load-deflection plots by varying the initial crack depth a_0/b ($G_{IC} = 0.01 \text{ kg/cm}$)

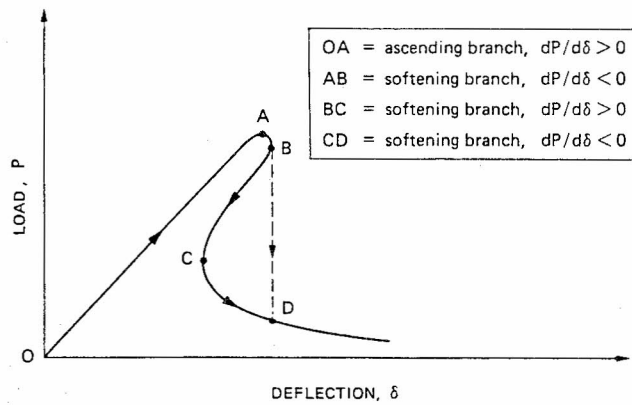


Figure 10. Snap-back softening behaviour

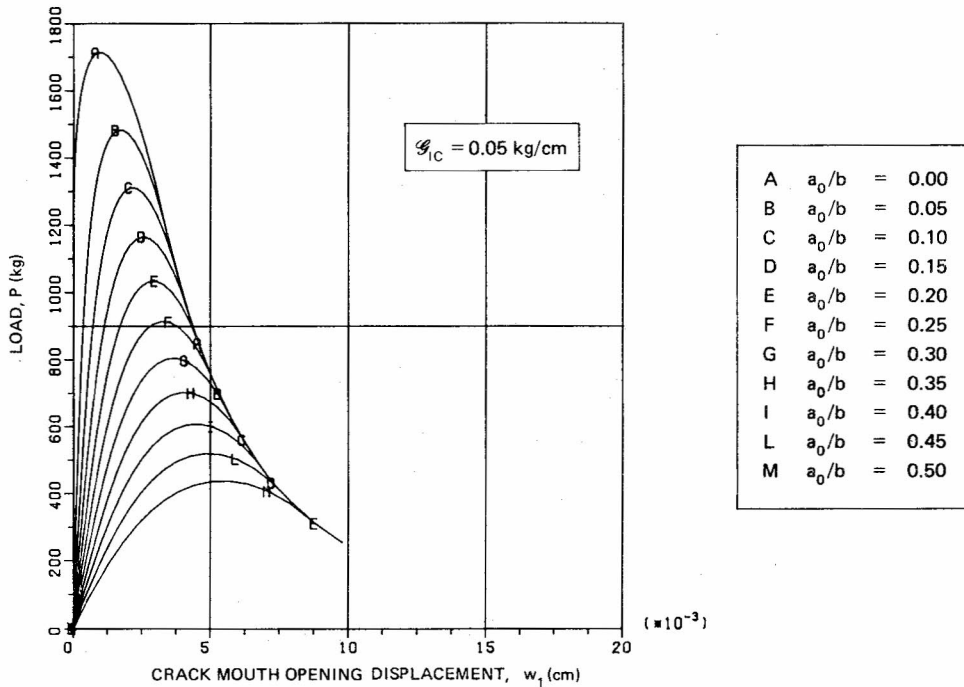


Figure 11. Load–crack mouth opening displacement plots by varying the initial crack depth a_0/b ($G_{IC} = 0.05 \text{ kg/cm}$)

coincide, so that a sharp bifurcation in the $P-\delta$ path is revealed, like that shown in Figure 9.

The catastrophic drop in the loading capacity may be avoided and the $P-\delta$ indentation experimentally evidenced by controlling the crack mouth opening displacement w_1 , instead of the beam deflection δ . In fact, as is shown in Figures 11 and 12, w_1 increases monotonically in the softening stage during the crack propagation.

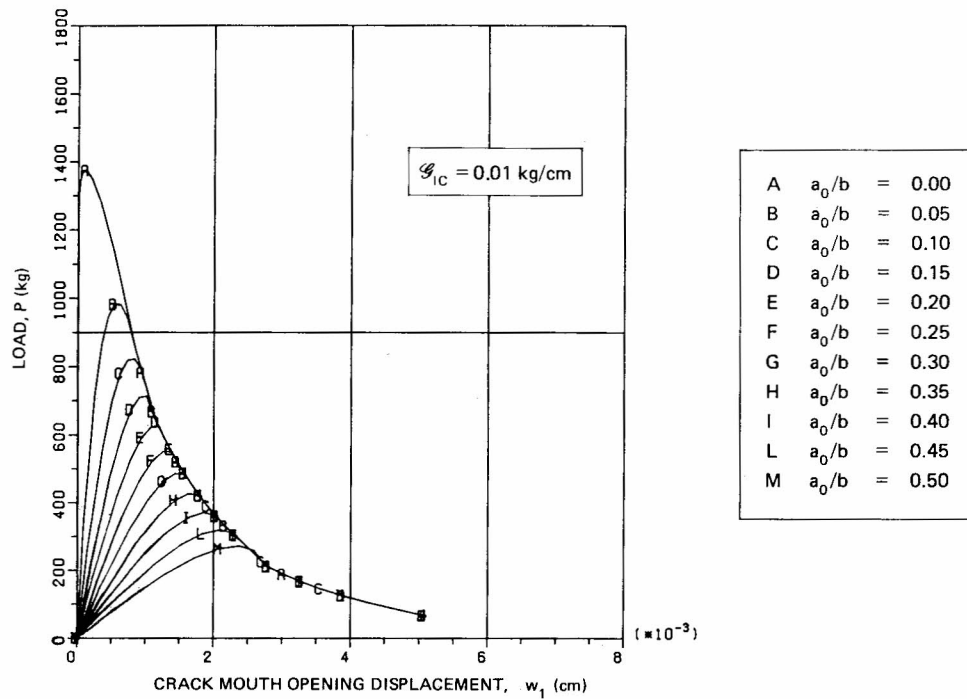


Figure 12. Load-crack mouth opening displacement plots by varying the initial crack depth a_0/b ($G_{IC} = 0.01$ kg/cm)

SIZE SCALE EFFECTS

The maximum loading capacity $P_{\max}^{(1)}$ according to the cohesive crack model is obtained from the $P-\delta$ diagrams in Figures 6 and 7. On the other hand, the maximum loading capacity $P_{\max}^{(2)}$ according to LEFM can be derived from the following formula:²⁵

$$P_{\max}^{(2)} = \frac{K_{IC} t b^{3/2}}{lg(a_0/b)} \quad (15)$$

with the shape-function g given by

$$g\left(\frac{a_0}{b}\right) = 2.9\left(\frac{a_0}{b}\right)^{1/2} - 4.6\left(\frac{a_0}{b}\right)^{3/2} + 21.8\left(\frac{a_0}{b}\right)^{5/2} - 37.6\left(\frac{a_0}{b}\right)^{7/2} + 38.7\left(\frac{a_0}{b}\right)^{9/2} \quad (16)$$

and the critical value of stress-intensity factor K_{IC} computed according to the well-known relationship (9).

Eventually, a simple ultimate strength analysis on the centre-line with the assumption of a linear stress variation through the ligament provides

$$P_{\max}^{(3)} = \frac{2 \sigma_u t (b - a_0)^2}{3 l} \quad (17)$$

The values of the ratios $P_{\max}^{(1)}/P_{\max}^{(2)}$ and $P_{\max}^{(3)}/P_{\max}^{(2)}$ are reported as functions of the inverse of the brittleness number s_E in Figure 13. As in the preceding section, the values $\varepsilon_u = 8.7 \times 10^{-5}$,

$t = b, l = 4b$ and $a_0 = 0.3b$ are assumed. The ratio $P_{\max}^{(1)}/P_{\max}^{(2)}$ may also be regarded as the ratio of the fictitious fracture toughness (given by the non-linear maximum load) to the true fracture toughness (considered as a material constant).

It is evident that, for high s_E numbers, the ultimate strength collapse results in a more critical condition than that of LEFM ($P_{\max}^{(3)} < P_{\max}^{(2)}$), as well as the results of the cohesive crack model tending to those of LEFM for low s_E values⁷

$$\lim_{s_E \rightarrow 0} P_{\max}^{(1)} = P_{\max}^{(2)} \tag{18}$$

It is interesting to observe that, for $s_E \lesssim 2 \times 10^{-5}$, the snap-back condition is predicted in the $P-\delta$ path (i.e. $dP/d\delta > 0$ in the softening stage) when the maximum load according to the cohesive crack model is higher than 80 per cent of that given by LEFM.

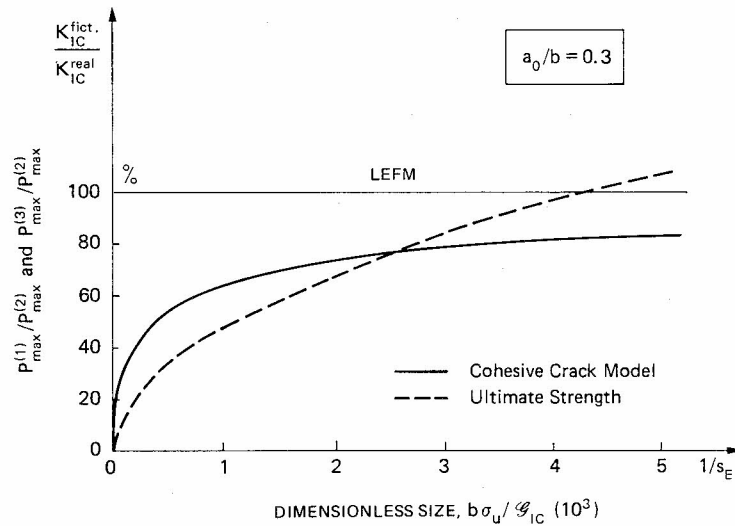


Figure 13. Transition from ultimate strength collapse at the ligament to LEFM crack instability, by varying the size scale of the structure

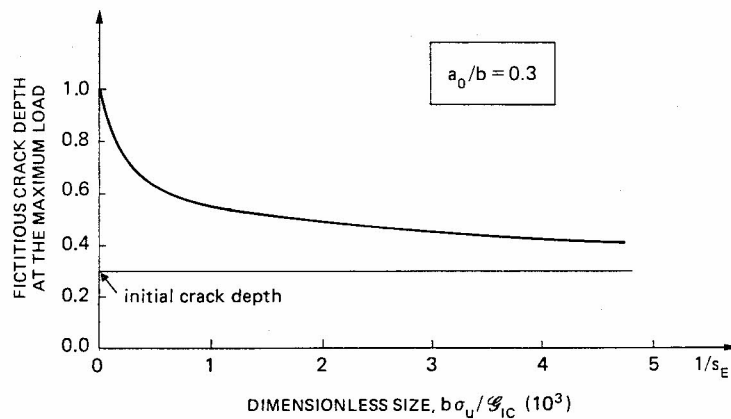


Figure 14. Fictitious crack depth at the maximum load as a function of the size scale of the structure

The fictitious crack depth at the maximum load is reported as a function of the inverse of the brittleness number s_E in Figure 14. The increase in the structure brittleness for $s_E \rightarrow 0$ is evident also from this diagram, the process zone at $dP/d\delta = 0$ tending to disappear, whereas it tends to cover the whole ligament for $s_E \rightarrow \infty$ (ductile collapse). The real (or stress-free) crack depth at the maximum load is nearly coincident with the initial crack depth for each value of s_E . This means that the slow crack growth does not start before the softening stage.

Recalling once again Figures 13 and 14, it is possible to state that, the smaller the brittleness number s_E is, i.e. the lower the fracture toughness, \mathcal{G}_{IC} , the larger the size scale b and/or the higher the ultimate tensile strength σ_u ($\varepsilon_u = \sigma_u/E$ being constant), the more accurate the snap-back instability in the P - δ path is in reproducing the classical LEFM instability.

CONCLUSIONS

1. The snap-back load-deflection branch may be identified only if the loading process is controlled by a monotonic increasing function of the crack length. In experiments the crack opening displacement is generally used for this purpose, whereas, in the numerical analysis, the crack length itself appears as the most natural driving parameter (crack length control scheme).
2. The maximum loading capacity can be predicted by LEFM and applying the simple condition $K_I = K_{IC}$, when $s_E \rightarrow 0$.
3. Neither the process zone develops nor the slow crack growth occurs before the catastrophic collapse, when $s_E \rightarrow 0$.
4. The finite element mesh must be exaggeratedly refined in order to determine the snap-back branch of the load-deflection path, when $s_E \rightarrow 0$.
5. The same conclusions can be drawn in the case of a non-linear σ - w cohesive law, as demonstrated in Reference 26.

ACKNOWLEDGEMENTS

The numerical results reported in the present paper were obtained in a joint research program between ENEL-CRIS-Milano and the University of Bologna.

REFERENCES

1. A. Carpinteri, 'Size effect in fracture toughness testing: a dimensional analysis approach', in G. C. Sih and M. Mirabile (eds.), *Proc. Int. Conf. on Analytical and Experimental Fracture Mechanics*, June 23-27, 1980, Roma, Sijthoff & Noordhoff, Amsterdam, 1981, pp. 785-797.
2. A. Carpinteri, 'Notch sensitivity in fracture testing of aggregative materials', *Eng. Fract. Mech.*, **16**, 467-481 (1982).
3. A. Carpinteri, C. Marega and A. Savori, 'Ductile-brittle transition by varying structural size', *Eng. Fract. Mech.*, **21**, 263-271 (1985).
4. A. Carpinteri and G. C. Sih, 'Damage accumulation and crack growth in bilinear materials with softening', *Theor. Appl. Fract. Mech.*, **1**, 145-159 (1984).
5. G. Maier, 'On the unstable behaviour in elastic-plastic beams in flexure' (in Italian), Istituto Lombardo, Accademia di Scienze e Lettere, *Rendiconti, Classe di Scienze (A)*, **102**, 648-677 (1968).
6. Z. P. Bažant, 'Instability, ductility and size effect in strain-softening concrete', *J. Eng. Mech. Div. ASCE*, **102**, 331-344 (1976).
7. A. Carpinteri, 'Interpretation of the Griffith instability as a bifurcation of the global equilibrium', in S. P. Shah (ed.), *NATO Advanced Research Workshop on Application of Fracture Mechanics to Cementitious Composites*, Evanston (Illinois), September 4-7, 1984, Martinus Nijhoff, Amsterdam, 1985, pp. 284-316.
8. M. A. Crisfield, 'Snap-through and snap-back response in concrete structures and the dangers of under-integration', *Int. j. numer. methods eng.*, **22**, 751-768 (1986).
9. H. Schreyer and Z. Chen, 'One-dimensional softening with localization', *J. Appl. Mech.*, **53**, 791-797 (1986).
10. J. G. Rots, D. A. Hordijk and R. de Borst, 'Numerical simulation of concrete fracture in direct tension', *Fourth Int.*

- Conf. on Numerical Methods in Fracture Mechanics*, San Antonio (Texas), March 23–27, 1987, Pineridge Press, Swansea, 1987, pp. 457–471.
11. C. Fairhurst, J. A. Hudson and E. T. Brown, 'Optimizing the control of rock failure in servo-controlled laboratory tests', *Rock Mech.*, **3**, 217–224 (1971).
 12. K. Rokugo, S. Ohno and W. Koyanagi, 'Automatic measuring system of load–displacement curves including post-failure region of concrete specimens', in F. H. Wittmann (ed.), *Fracture Toughness and Fracture Energy of Concrete, Proc. Int. Conf. on Fracture Mechanics of Concrete*, Lausanne (Switzerland), October 1–3, 1985, Elsevier, Amsterdam, 1986, pp. 403–411.
 13. L. Biolzi, S. Cangiano, G. P. Tognon and A. Carpinteri, 'Snap-back softening instability in high strength concrete beams', *SEM-RILEM Int. Conf. on Fracture of Concrete and Rock*, Houston (Texas), June 17–19, 1987 (*Materials & Structures*, in press).
 14. G. I. Barenblatt, 'The formation of equilibrium cracks during brittle fracture. General ideas and hypotheses. Axially-symmetric cracks', *J. Appl. Math. Mech.*, **23**, 622–636 (1959).
 15. D. S. Dugdale, 'Yielding of steel sheets containing slits', *J. Mech. Phys. Solids*, **8**, 100–104 (1960).
 16. B. A. Bilby, A. H. Cottrell and K. H. Swinden, 'The spread of plastic yield from a notch', *Proc. R. Soc.*, **A272**, 304–314 (1963).
 17. J. R. Rice, 'A path independent integral and the approximate analysis of strain concentration by notches and cracks', *J. Appl. Mech.*, **35**, 379–386 (1968).
 18. M. P. Wnuk, 'Quasi-static extension of tensile crack contained in a viscoelastic–plastic solid', *J. Appl. Mech.*, **41**, 234–242 (1974).
 19. A. Hillerborg, M. Modeer and P. E. Petersson, 'Analysis of crack formation and crack growth in concrete by means of fracture mechanics and finite elements', *Cement Concrete Res.*, **6**, 773–782 (1976).
 20. A. R. Ingraffea, 'Theory of crack initiation and propagation in rock', in B. Atkinson (ed.), *Rock Fracture Mechanics*, Academic Press, New York, 1987, Chapter 3.
 21. P. E. Petersson, 'Crack growth and development of fracture zones in plain concrete and similar materials', *Report TVBM-1006*, Division of Building Materials, Lund Institute of Technology, 1981.
 22. G. Colombo and E. Limido, 'Un metodo numerico per l'analisi di prove TPBT stabili: confronto con alcuni dati sperimentali', *XI Convegno Nazionale dell'Associazione Italiana per l'Analisi delle Sollecitazioni*, Torino, 1983, pp. 233–243.
 23. A. Carpinteri, A. Di Tommaso and M. Fanelli, 'Influence of material parameters and geometry on cohesive crack propagation', in F. H. Wittmann (ed.), *Fracture Toughness and Fracture Energy of Concrete, Proc. Int. Conf. Fracture Mechanics of Concrete*, Lausanne (Switzerland), October 1–3, 1985, Elsevier, Amsterdam, 1986, pp. 117–135.
 24. Z. P. Bažant and P. A. Pfeiffer, 'Determination of fracture energy from size effect and brittleness number', *ACI Mater. J.*, **85**, 463–480 (1987).
 25. Standard Method of Test for Plane Strain Fracture Toughness of Metallic Materials, *E 399-74*, ASTM.
 26. A. Carpinteri, G. Colombo, G. Ferrara and G. Giuseppetti, 'Numerical simulation of concrete fracture through a bilinear softening stress-crack opening displacement law', in S. P. Shah and S. E. Swartz (eds.), *Proc. SEM-RILEM Int. Conf. on Fracture of Concrete and Rock*, Houston (Texas), June 17–19, 1987, pp. 178–191.